Defects in Carbon-Rich Ferrite of Cold-Drawn Pearlitic Steel Wires

Y.Z. CHEN, G. CSISZÁR, J. CIZEK, S. WESTERKAMP, C. BORCHERS, T. UNGÁR, S. GOTO, F. LIU, and R. KIRCHHEIM

By means of X-ray line profile analysis and positron lifetime spectroscopy, densities of deformation-induced defects in carbon-rich ferrite of a series of cold-drawn pearlitic steel wires with true strains (ε) up to 5 are characterized. It is shown that both the dislocation densities and the vacancy cluster concentrations increase continuously with increasing ε. On the basis of the measured defect densities, values of defect hardening are estimated. The result shows that contributions of the defect hardening to the total tensile strength of the wires reach nearly 40 pct, which is mainly ascribed to the dislocation hardening. Chemical surroundings of the defects in the carbon-rich ferrite are investigated by coincidence Doppler broadening spectroscopy. The association of carbon with the defects in ferrite is demonstrated.

DOI: 10.1007/s11661-013-1723-x

I. INTRODUCTION

COLD-DRAWN pearlitic steel wires, with extremely high strength and tolerant ductility, have been used widely in engineering applications, such as tire cords, springs, suspension bridges, *etc*., and studied extensively for many years.[1–15] These wires are produced by cold-drawn patented pearlitic steel wires, which are composed of ferrite and cementite lamellae, to a defined strain. Upon cold-drawing, the cementite lamellae are partially decomposed,[5–13] while numerous lattice defects, such as dislocations and vacancies or vacancy clusters, are introduced into the ferrite lamellae.[14] Since both the dislocations and the vacancies or vacancy clusters cause hardening,[16] these defects present in high densities may play a crucial role in strengthening the wires. Thus, a systematic investigation of the evolution of defect densities in ferrite lamellae with changing true strain (ε) will be helpful in understanding the strengthening mechanisms of the wires. After deformation, a large number of carbon atoms stemming from the decomposed cementite are released into ferrite.[6–13] Since the equilibrium solubility of carbon in ferrite at room temperature is merely several atomic ppm, it has been suggested that the carbon in ferrite is probably associated with the defects in ferrite.[8,13] However, the association of carbon with defects in these wires still lacks direct experimental evidence. Although atom probe tomography is capable of mapping carbon atmospheres around dislocations,[17,18] the extremely high dislocation density and the extremely fine width of ferrite lamellae prevent a precise mapping of carbon atmospheres at dislocations in this special case.[13] An investigation of the accommodation of carbon in ferrite requires other methods.

A combination of X-ray line profile analysis (XLPA) and positron annihilation spectroscopy (PAS) has been a successful method applied by the authors to quantitatively characterize defect densities in ferrite of cold-drawn pearlitic steel wires.[14] However, that study was performed only on wires with the true strains of $\varepsilon = 0$ and 3, and intended to show the evidence of high density of vacancy clusters existing in ferrite of the latter. In the current study, combined investigations of XLPA and PAS are extended to a series of cold-drawn pearlitic steel wires with true strains $\varepsilon = 0$ to 5, by adding analyses for $\varepsilon = 1$, 2, 4, and 5 to those for $\varepsilon = 0$ and 3 reported previously.[14] Coincidence Doppler broadening spectroscopy (CDBS) is a powerful tool to study chemical surrounding of lattice defects.[16] Therefore, CDBS is employed to characterize the chemical surrounding of these defects to demonstrate the association of carbon with the defects in ferrite.

II. EXPERIMENTAL

The steel wires used in the current study were provided by Nippon Steel Corporation. The chemical

Y.Z. CHEN, Associate Professor, is with the State Key Laboratory of Solidification Processing, Northwestern Polytechnical University, 710072 Xi'an, P.R. China and also with the Institut für Materialphysik, Universität Göttingen, 37077 Göttingen, Germany. Contact e-mail: yzchen@nwpu.edu.cn G. CSISZÁR, Post-Doc, and T. UNGÁR, Full Professor, are with the Department of Materials Physics, Eötvös University, Budapest 1518 POB, Hungary. J. CIZEK, Associate Professor, is with the Department of Low-Temperature Physics, Charles University in Prague, V Holesovickach 2 18000 Praha 8, Czech Republic. S. WESTERKAMP, Graduate Student, and C. BORCHERS, Research Scientist, are with the Institut für Materialphysik, Universität Göttingen. S. GOTO, Full Professor, is with the Department of Materials Science and Engineering, Akita University, Akita, 010-8502, Japan. F. LIU, Full Professor, is with the State Key Laboratory of Solidification Processing, Northwestern Polytechnical University. R. KIRCHHEIM, Full Professor, is with the Institut för Materialphysik, Universität Göttingen, and also with the International Institute for Carbon–Neutral Energy Research (WPI-I2CNER), Kyuchu University, Fukuoka, Japan.

Manuscript submitted June 15, 2011.
Article published online April 10, 2013

composition of the material is listed in Table I. Processing procedures of the wires are described elsewhere.[7] During the cold-drawing process, temperature of the wires did not exceed 373 K (100 °C).

High energy X-ray diffraction measurements with Co-Kα radiation were performed following the procedures described in Reference 19 to measure the XRD patterns for XLPA. The contribution of Co-Kα2 was blocked by a proper slit. The wires were bundled to achieve a sufficiently large area exposed to the X-ray beam. Since the ferrite lamellae have a strong $\langle 110 \rangle$ texture along the wire-drawing direction, only (110) plane of ferrite lamellae can be observed in the transverse cross sections of the wires.[7] However, the pearlitic lamellae show a strong wavy structure in the transverse cross sections.[10] Therefore, XRD measurements performed on the longitudinal cross sections of the wires will be helpful to reduce the effect of preferred crystallographic orientation. The specimens were irradiated for 24 h to achieve sufficient statistics in XRD patterns. An imaging-plate detector was used to record Debye–Scherrer rings. As shown in Figure 1, the intensity along the Debye–Scherrer ring corresponding to each Bragg reflection of ferrite is quite homogeneous, indicating a substantial reduction of the effect of preferred crystallographic orientation. XRD line profiles were obtained by integrating the whole measured Debye–Scherrer rings.

PAS measurements were performed following same procedure as described in References 14, 20, 21 Carrier-free[22] Na_2CO_3 with an activity of 1 MBq encapsulated between 2-μm mylar foils was used as a positron source. Since the ground-state energy of positrons in ferrite is lower than that in cementite and the mean diffusion length of positrons in transition metals is two orders of magnitude larger than the observed width of cementite lamellae in cold-drawn pearlitic steel wires, positrons annihilate dominantly in ferrite.[14] This guarantees the applicability of the current positron annihilation techniques (PAS and CDBS) for investigating defects in ferrite.

Table I. Chemical Composition of Pearlitic Steel Wires (Weight Percent)

C	Si	Mn	P	S
0.82	0.20	0.50	0.005	0.004

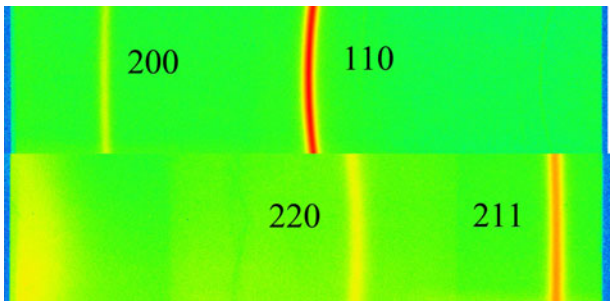

Fig. 1—A typical measured Debye–Scherrer pattern (ε = 3).

CDBS measurements were carried out with an apparatus equipped with two high-purity germanium (HPGe) detectors.[22] The spectrometer allows for an overall energy resolution of 0.9 keV (FWHM) at 511 keV energy. The peak-to-background ratio was around 10^6. CDBS measurements were performed using the same positron source as the one used in the PAS investigations. At least 10^8 counts were collected in each two-dimensional γ-ray energy spectrum. The spectrum was then reduced to one-dimensional cuts representing the Doppler-broadened profile (DBP) and the resolution function of the spectrometer. The DBPs were described in terms of the ratios of DBP cuts to that of a pure Fe reference material.

III. RESULTS AND DISCUSSION

A. *Evolution of Defect Densities and Defect Hardening*

1. *Evolution of dislocation density*

XRD line profiles of the wires are shown in Figure 2, where the Bragg peaks of ferrite broaden as ε increases. The conventional and modified Williamson–Hall plots for ferrite with different ε are presented in Figures 3(a) and (b). The axis labels K and ΔK are defined as $K = 2\sin\theta/\lambda$ and $\Delta K = 2\Delta\theta\cos\theta/\lambda$ with θ the Bragg angle, $\Delta\theta$ the FWHM (full width at half maximum), both measured in radians from the XRD line profiles, λ the wave-length of the X-ray source, and C the dislocation contrast factor which is defined by Ungár and his colleagues.[23,24] If the microstrain* stored in ferrite is isotropic, ΔK (representing the broadening of each Bragg peak) *vs* K (corresponding to each Bragg reflection) will be linear in the conventional Williamson–Hall plots. However, it is found that for each wire, ΔK *vs* K is not linear, and the deviations of the data points

*Microstrain refers to the local lattice strain around dislocation cores.

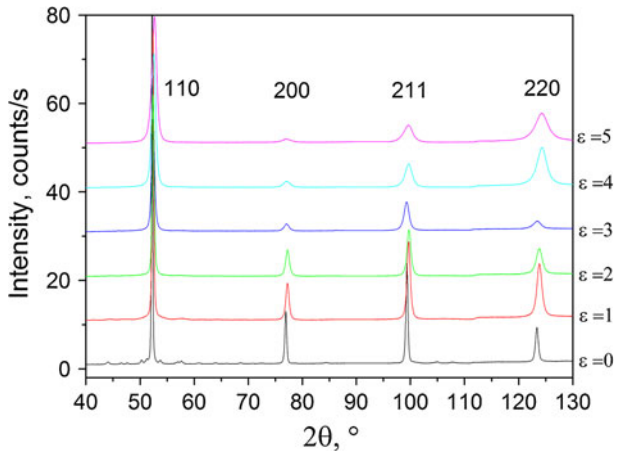

Fig. 2—XRD line patterns of the wires. In order to distinguish each pattern, the upper pattern is shifted vertically by 10 counts/s from the pattern below.

from a straight line become more pronounced with increasing ε, see Figure 3(a), which indicates that the broadenings of Bragg peaks with respect to different Bragg reflections are anisotropic. The anisotropic peak broadening observed in these wires (Figure 3(a)) can be caused by the microstrain anisotropy in plastically deformed cubic metals.[24] The microstrain anisotropy observed in this case is suggested to be ascribed to dislocations, where the anisotropic strain field of single dislocations and the effective cut-off radius R play a role.[24] The microstrain anisotropy (*i.e.*, the zig-zag variation in Figure 3(a)) can be removed by introducing the dislocation contrast factor (C) in modified Williamson–Hall plots.[24,25] The principle and procedure in constructing the modified Williamson–Hall plots are presented in Appendix. It is shown in the modified Williamson–Hall plots (Figure 3(b)) that, for all the wires, ΔK and $KC^{1/2}$ can converge into a straight line,

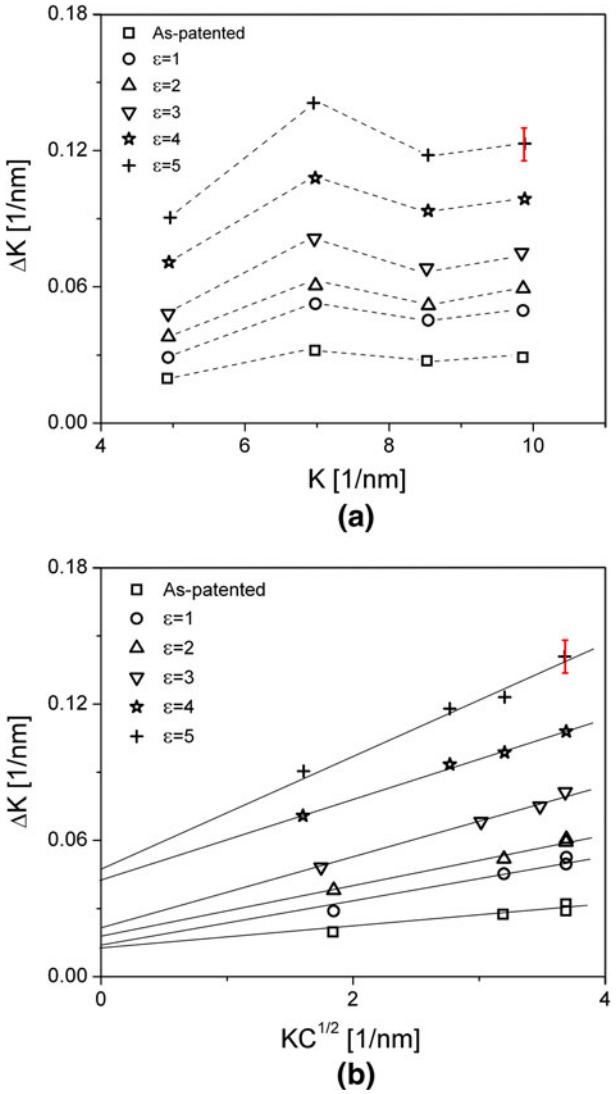

Fig. 3—(*a*) The conventional Williamson–Hall plots and (*b*) the modified Williamson–Hall plots for ferrite at different ε. The standard error bar in determination of FWHM is shown in the last reflection of $\varepsilon = 5$ in (a) and (b).

which demonstrates the appropriateness of the currently applied XLPA. On the other hand, since the intercepts at the ΔK-axis and the slopes of the modified Williamson–Hall plots increase with increasing ε, the results indicate a refinement of the ferrite lamellae and an increase of dislocation density (ρ) upon cold-drawing.

Applying the standard eCMWP fitting procedures developed on the basis of Fourier transform method,[26–28] the X-ray line profiles are further quantitatively analyzed. The physical parameters used in eCMWP fitting are available in Reference 14 Figure 4 gives an example of an eCMWP fitting, revealing a perfect fitting by the applied analysis. The structural parameters obtained from the eCMWP fitting are listed in Table II. The area-weighted mean crystallite size $\langle x \rangle_{\text{area}} = m \exp(2.5\sigma^2)$($m$ and σ are the median and the variance of the crystallite size distribution, respectively) can be determined by the structure parameters derived from the eCMWP fitting. As shown in Table II, with increasing strain ε, $\langle x \rangle_{\text{area}}$ decreases continuously, while the dislocation density ρ increases. When ε attains 4 and 5, ρ reaches the order of 10^{16} m^{-2}, which corresponds to its saturation value in Fe.[29] The dislocation densities obtained in the current study are in the same order of magnitude as the values determined by TEM in a recent report.[30] q parameter represents the character of dislocations (*e.g.*, edge or screw type).[31,32] According to Reference 32, $q = 2.0 \pm 0.2$ indicates a mixed character of edge- and

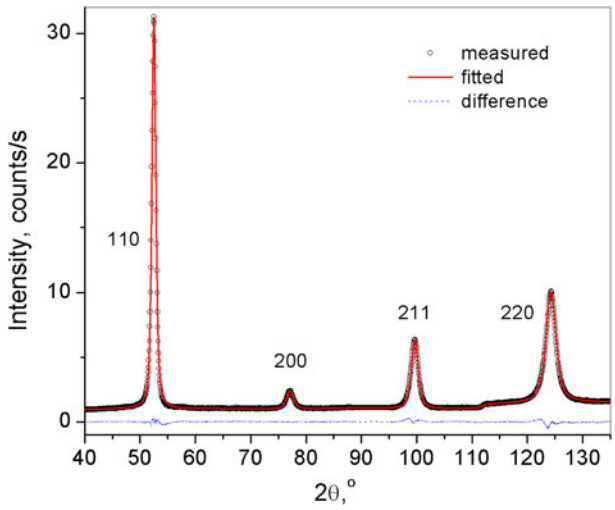

Fig. 4—Typical measured (open circles) and fitted (solid lines) patterns ($\varepsilon = 4$). Dotted line in the bottom is the difference between the measured and fitted data.

Table II. Parameters Obtained by the eCMWP Analyses

ε	m (nm)	σ	$\langle x \rangle_{\text{area}}$ (nm)	ρ (10^{15} m^{-2})	q
0	37	0.40	55	0.8 (±0.2)	2.1 (±0.2)
1	29	0.36	40	3.8 (±0.5)	2.1 (±0.2)
2	26	0.28	31	4.8 (±0.6)	2.0 (±0.2)
3	13	0.39	19	8.0 (±1.0)	2.2 (±0.2)
4	10	0.33	13	12.0 (±1.5)	2.5 (±0.2)
5	8	0.37	11	13.0 (±1.5)	2.5 (±0.2)

screw-type dislocations for $\varepsilon = 0$ to 3, and $q = 2.5 \pm 0.2$ suggests that for $\varepsilon = 4$ and 5, screw-type dislocations are dominant.

2. *Evolution of vacancy cluster concentration*

Figures 5(a) and (b) show the results of positron lifetime measurements of the wires. Three components with lifetimes τ_1, τ_2, and τ_3, corresponding to free positrons, positrons trapped at dislocations, and positrons trapped at vacancy clusters, respectively,[14] are resolved in the positron lifetime spectra. The free-positron component with the lifetime τ_1 and the relative intensity I_1 is only detected for $\varepsilon = 0$ and 1, see Figure 5(a), but not for the higher strains. The second component, which stems from the positrons trapped at dislocations, is the main contribution in the lifetime spectra. It has an approximately constant lifetime τ_2 and its intensity accounts for 80 to 90 pct of the total intensity, see Figure 5(b). A long-living component with the lifetime τ_3, stemming from the vacancy clusters, is detected except for in the as-patented wire. It should be noted that the vacancy clusters observed from the positron lifetime spectra are expected to have a shape of more or less spherical nanovoids. If vacancies agglomerate in a same plane, then the collapse of these vacancies will lead to the formation of dislocation loops.[16] The positrons trapped at dislocation loops will have a lifetime as those trapped at dislocations τ_2, and the long-living component with lifetime τ_3 will not be detected. Since the lifetime of positrons trapped in vacancy clusters increases with increasing size of the vacancy clusters,[33] the results shown in Figure 5(a) indicate that the size of the vacancy clusters remains approximately constant for $\varepsilon \leq 3$ and increases when $\varepsilon > 3$. According to theoretical calculations,[34,35] the number of vacancies contained in the vacancy clusters can be estimated roughly as 9 ± 1 for $\varepsilon \leq 3$, 10 ± 1 for $\varepsilon = 4$, and 15 ± 1 for $\varepsilon = 5$.

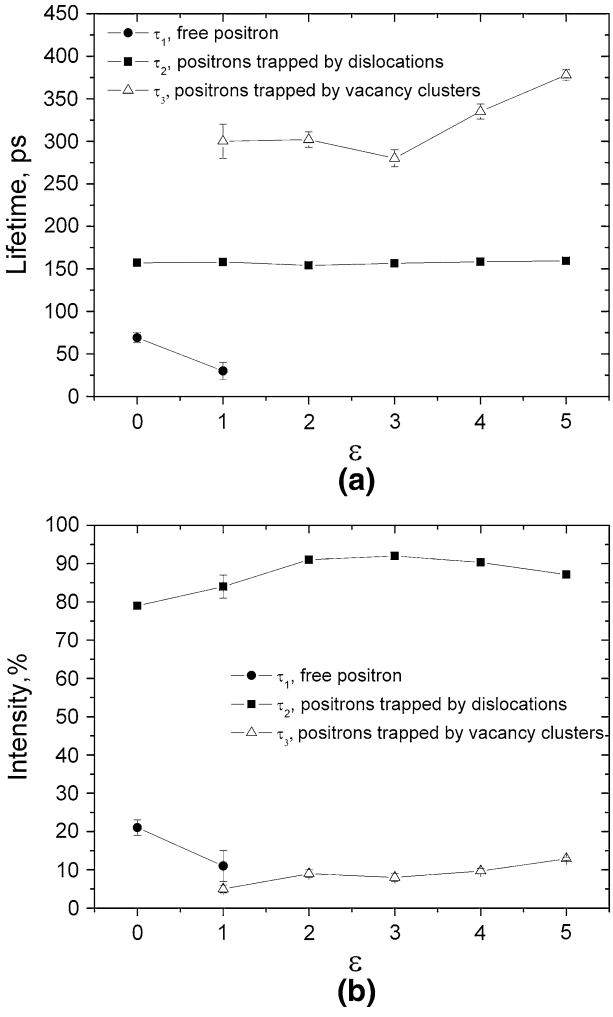

Fig. 5—(*a*) Measured positron lifetime (τ_i) and (*b*) measured relative intensity (I_i) corresponding to different components as a function of ε. The data corresponding to $\varepsilon = 0$ and 3 are cited from Ref. [14].

Because of the existence of the free positron component for $\varepsilon = 0$ and 1, the concentration of the vacancy clusters (c_{VC}) can be calculated with a three-component trapping model[35]:

$$c_{VC} = \frac{\left(\frac{1}{\tau_B} - \frac{I_2}{\tau_2} - \frac{1-I_2}{\tau_3}\right) I_3}{I_1 \nu_{VC}}, \quad [1]$$

where $\tau_B = 108$ ps is the positron lifetime in well-annealed Fe;[36] ν_{VC} is the specific positron trapping rate for the vacancy cluster and can be calculated by $\nu_{VC} = N \cdot \nu_V$, where N is the number of vacancies in each vacancy cluster; and ν_V is the specific positron trapping rate of a monovacancy.[37] For $\varepsilon > 1$, all positrons are trapped at the lattice defects. Thus, c_{VC} can be calculated by[14]

$$c_{VC} = \frac{\nu_D}{\nu_{VC}} \frac{I_3}{I_2} \rho, \quad [2]$$

where ν_D is the specific positron trapping rate at dislocations and equals to $(2.0 \pm 1.0) \times 10^{-5}$ m^2 s^{-1} in ferrite of pearlitic steels.[14] Using $\nu_V = (1.1 \pm 0.2) \times 10^{15}$ s^{-1} reported by Vehanen *et al.*,[36] ν_{VC} can be taken as $(10 \pm 2) \times 10^{15}$ s^{-1} for $\varepsilon \leq 3$, $(11 \pm 2) \times 10^{15}$ s^{-1} for $\varepsilon = 4$, and $(17 \pm 3) \times 10^{15}$ s^{-1} for $\varepsilon = 5$. Substituting the values of ρ listed in Table II and the measured positron lifetimes and intensities shown in Figures 5(a) and (b) into Eqs. [2] and [3] into Eqs. [1] and [2], c_{VC} can be calculated, see Figure 6. Here too, c_{VC} increases with increasing ε. As discussed before,[14] the value of ν_V reported for monovacancies in Fe by Vehanen *et al.*[36] is rather high and around one order of magnitude higher than for many other transition metals.[38–43] Assuming that ν_V holds a value of only 2×10^{14} s^{-1} which is in the same order of the values reported in many other transition metals,[38–43] c_{VC} will be about five times higher than the values determined with $\nu_V = (1.1 \pm 0.2) \times 10^{15}$ s^{-1}, as depicted in Figure 6.

3. *Defect hardening*

Strengthening mechanisms of the cold-drawn pearlitic steel wires have been investigated extensively for many years.[1–3,7,8,16,30,44] However, because of complex interplay among the factors involved in strengthening of the wires, the mechanism has not been fully understood yet.

As mentioned above, both dislocations and vacancy clusters are believed to play important roles in hardening the wires. Using the defect densities determined above, the amount of hardening due to the dislocations and the vacancy clusters in ferrite can be estimated. This is, however, only a certain fraction of the total strength. For instance, the hardening effect caused by the interaction between dislocations and carbon is not evaluated here, because a highly complex scenario of dislocation locking and unlocking by carbon is expected in steel.[16,45]

Dislocation-induced flow stress ($\Delta\sigma_D$) can be related to the dislocation density by Taylor equation,[16]

$$\Delta\sigma_D = M\alpha Gb\rho^{1/2} \quad [3]$$

where $M = 1.84$ is the Taylor factor,[30] $\alpha = 0.24$ is a constant,[46] G is the shear modulus (80 GPa), and b is the magnitude of the Burgers vector (0.248 nm). Using Eq. [3] and the values of ρ listed in Table II, $\Delta\sigma_D$ can be calculated, see Table III. The results show that $\Delta\sigma_D$ increases continuously from 248 MPa to 1000 MPa as ε rises.

Hardening effect by vacancy clusters is suggested to be similar to dispersion hardening by Zehetbauer.[47] According to Reference 16, the interaction between dislocations and dispersed particles follows two different mechanisms, *i.e.*, *cutting through* the particles in the case of small particles and *bowing out* around the particles in the case of large particles. For metals, typical critical radii of the particles leading to the transition from one interaction mechanism to the other are between 2.5 and 25 nm.[16] As mentioned in Section III–A–2, the vacancy clusters in ferrite contain around 10 vacancies. The radius of these clusters corresponds to $r_{VC} = (3a_0^3N/8\pi)^{1/3} = 0.3$ nm with the lattice parameter $a_0 = 0.2866$ nm, and the number of vacancies containing in each vacancy cluster $N = 10$.[48] This value is smaller than the lower limit of the critical radii mentioned above. Therefore, the *cutting-through* mechanism should work. Then, assuming a homogeneous distribution of the vacancy clusters in ferrite, the hardening effect can be estimated by[16]

$$\Delta\sigma_{VC} = \frac{\gamma L}{br_{VC}} = \frac{\gamma(N_A c_{VC}/V_m)^{1/3}}{br_{VC}} \quad [4]$$

where $\gamma = 2.32$ J/m^2 is the surface energy of vacancy cluster/micro-void in Fe,[48] L is the mean distance between particles, N_A is the Avogadro number, and V_m is the molar volume of Fe. Using c_{VC} shown in Figure 6, $\Delta\sigma_{VC}$ can be calculated and the values are listed in Table III. The magnitude of $\Delta\sigma_{VC}$ rises continuously from 0 to about 200–300 MPa, the uncertainty is, however, quite large.

The estimations shown in Table III indicate that, as ε increases, the increase of strength by the defect hardening is enhanced continuously, because of the increase of the defect densities in ferrite. The dislocations play a more significant role in strengthening of the wires than the vacancy clusters. Hence, the uncertainty in $\Delta\sigma_{VC}$ is not important. After deformation, the defect hardening contributes pronouncedly to the tensile strength of the wires and reaches nearly 40 pct of the total strength in some wires. It should be kept in mind that other strengthening effects such as Hall–Petch strengthening or solid-solution hardening also have important contributions to strengthening the wires, but are beyond the scope of this report.

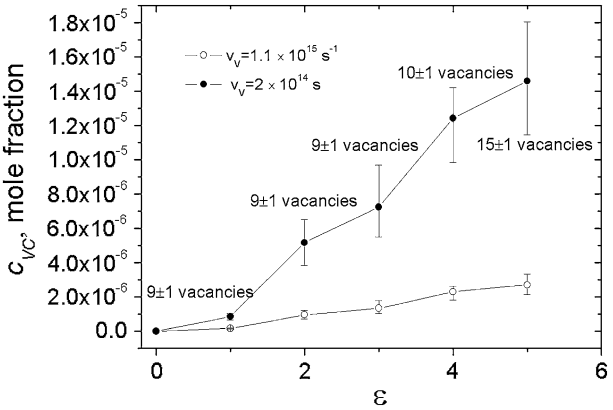

Fig. 6—PAS determined c_{VC} as a function of ε. The data corresponding to $\varepsilon = 0$ and 3 are cited from Ref. [14].

B. *Segregation of Carbon Atoms at Defects in Ferrite*

The curves of coincidence Doppler-broadening (CDB) ratio related to ferrite of the wires with different ε are shown in Figure 7(a). The shapes of these curves are similar to that of the defect-free reference (pyrolytic

Table III. Measured Tensile Strength and Estimated Contributions Due to the Defect Hardening

ε	Tensile Strength (MPa)	Dislocation Hardening, $\Delta\sigma_D$ (MPa)	Vacancy Cluster Hardening, $\Delta\sigma_{VC}$ (MPa)	The Fraction of the Strength Induced by Defect Hardening in the Total Tensile Strength
0	1300	248	0	19 pct
1	1700	540	67 to 118	36 to 39 pct
2	2000	607	123 to 215	37 to 41 pct
3	2700	784	137 to 240	34 to 38 pct
4	3550	960	164 to 288	32 to 35 pct
5	4500	1000	173 to 304	26 to 29 pct

In the last column of the table, the total tensile strength refers to the tensile strength of the wires listed in the first column.

graphite) in the high momentum regime ($p > 10 \times 10^{-3}\ m_0c$), which implies that a pronounced fraction of the positrons are annihilated by the electrons bound to carbon atoms. In the low momentum range ($p < 10 \times 10^{-3}\ m_0c$), the shapes of the curves differ. In contrast to the pyrolytic graphite, in the wires, most positrons are trapped at the defects in ferrite. The positrons trapped at these defects enhance the low-momentum part and reduce the contribution of those annihilated with the high-momentum core electrons. The solid line in Figure 7(a) represents the curve for the pyrolytic graphite rescaled by the factor ξ_C, which represents the fraction of the positrons annihilated by electrons bound to carbon atoms. In the pyrolytic graphite, obviously $\xi_C = 100$ pct, while in the wires, ξ_C increases from 25 pct for $\varepsilon = 0$ to 54 pct for $\varepsilon = 5$, see Figure 7(b).

In a defect-free alloy where solute atoms are distributed homogeneously, the number of positrons annihilated with electrons bound to solute atoms is equal roughly to the number of the solute atoms.[49] However, the observed values of ξ_C are much higher than the carbon concentration in the ferrite ranging from of 0.5 to 1.7 at. pct measured by atom probe tomography.[13] As mentioned above, virtually all positrons are trapped at the lattice defects in ferrite for $\varepsilon > 1$. If these defects are decorated with carbon atoms, then the probability of the positrons to annihilate with the electrons bound to carbon atoms will be significantly enhanced, resulting in a large ξ_C. Therefore, the large values of ξ_C shown in Figure 7(b) provide the direct evidence for the decoration of carbon atoms with the lattice defects in ferrite. The already large value of ξ_C, 25 pct, observed in the as-patented wire means that the dislocations in the as-patented wires are decorated with carbon atoms as well. Upon wire drawing, the defect densities and, concomitantly, ξ_C, increase continuously, indicating that these defects are decorated with the carbon atoms released from the decomposed cementite.

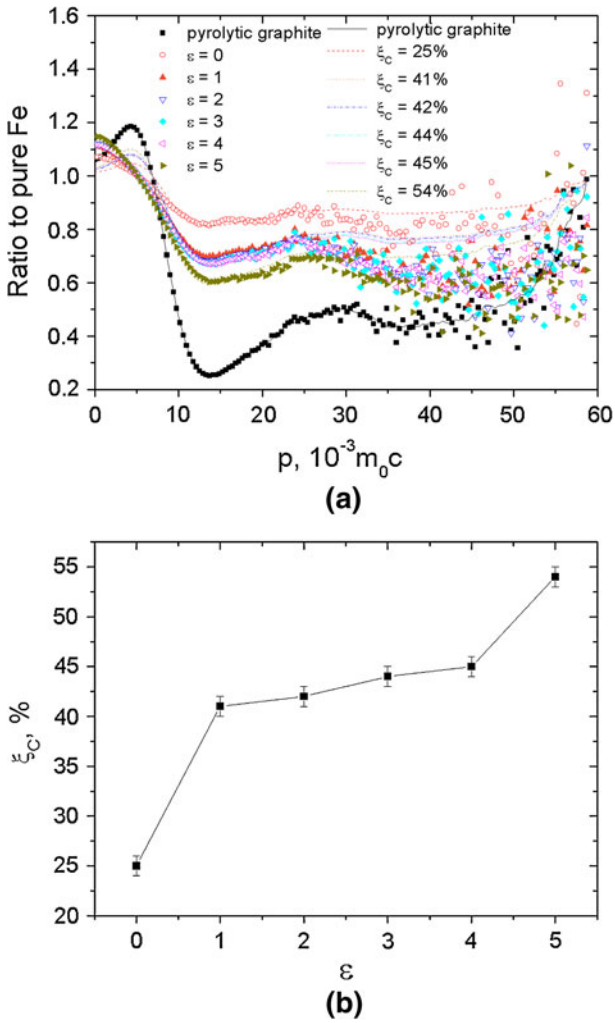

Fig. 7—(*a*) Curves of CDB ratio related to ferrite of the wires, where ξ_C and p are the fractions of the positrons annihilated by the electrons bound to carbon atoms and electron momentum, respectively. m_0c is the unit of electron momentum with m_0 being the mass of phonon, and c the speed of light. (*b*) ξ_C *vs* ε.

IV. CONCLUSIONS

The evolution of defect densities in carbon-rich ferrite of cold-drawn pearlitic steel wires drawn to different strains ε were studied systematically by means of XLPA and PAS. Defect hardening values due to the dislocations and the vacancy clusters in ferrite were estimated. Chemical surroundings of the defects were investigated by CDBS. Segregation of the carbon atoms to the defects in ferrite was discussed accordingly. The conclusions drawn in the current study are summarized as follows:

(1) Both the dislocation densities and the vacancy cluster concentrations are found to increase continuously as ε increases. The dislocation densities and the vacancy cluster concentrations reach the orders of 10^{16} m^{-2} and 10^{-6} to 10^{-5}, respectively, at the true strain $\varepsilon \geq 4$.
(2) Hardening by dislocations and vacancy clusters contributes to the strengthening of the wires by a large amount. The overall contribution of the defect hardening to the total tensile strength is mainly attributed to the dislocation hardening. The effect of the vacancy clusters hardening is rather weak.
(3) Pronounced segregation of carbon atoms to the defects in ferrite is verified by the CDBS investigations.

ACKNOWLEDGMENTS

The authors gratefully acknowledge the financial supports from the Deutsche Forschungsgemeinschaft (SFB 602 TP B13 and KI 230/34), the Alexander von Humboldt Stiftung, the Czech Science agency (project P108/12/G043), and thank Prof. D. Raabe, Dr. Y.J. Li,

and Dr. P. Choi for fruitful discussions, as well as Dr. S. Nishida from Nippon Steel Company for providing the wire specimens. Y.Z.C. appreciates the supports from the Natural Science Foundation of China (Nos. 51101121 and 51125002), the Research Fund of the State Key Lab. of Solidification Processing (NWPU) (No. 79-TP-2011), and the Fundamental Research Fund of NWPU (No. JC2001134). G.Cs. and T.U. are grateful to the Hungarian National Science Foundation (OTKA #71594, #67692 and #80772) for the supports provided for the x-ray peak profile analysis.

APPENDIX

According to a model proposed by Ungár *et al.*,[31] the dislocation contrast factor (C) for Bragg reflection hkl can be calculated by

$$C = C_{h00}(1 - qH^2) \qquad [A1]$$

where C_{h00} is the average dislocation contrast factor for Bragg reflection $h00$, q is a parameter depending on the character of dislocations (*e.g.*, edge or screw type), and $H^2 = (h^2k^2 + h^2l^2 + k^2l^2)/(h^2 + k^2 + l^2)^2$ with h, k, and l are the Miller indices. C_{h00} has been modeled by Ungár *et al.*[31] and can be computed by means of a program named *ANIZC* developed by Borbély *et al.*[50] Assuming edge dislocations and screw dislocations present in equal proportions in the material, using the *ANIZC* program,[50] C_{h00} is computed as 0.256 for ferrite.[14] q parameter can be obtained by either a least-square fitting on experimentally determined ΔK and K to achieve a linear relationship between ΔK and $KC^{1/2}$ or by the standard eCMWP (extended Convolutional Multiple Whole Profile) fitting procedures[26–28] employed in the second paragraph of Section III–A–1. Practically, C_{h00} in Eq. [A1] is a pre-factor for C and simply assumes all types of dislocations present in equal proportions, while q is a parameter determined experimentally and represents the character of dislocations. The combination of C_{h00} and q in Eq. [A1] gives the weights of different types of dislocations in C. A proper value of q parameter gives proper values of C for Bragg refection hkl, which have to smoothen the anisotropic peak broadening at different Bragg reflections, *i.e.*, ΔK increases linearly with $KC^{1/2}$. Using $C_{h00} = 0.256$ and the values of q parameter determined by eCMWP fitting procedure below, C can be calculated by Eq. [A1] for ferrite of the wires. On this basis, the modified Williamson–Hall plots are obtained, see Figure 3(b).

REFERENCES

1. T. Takahashi, I. Ochiai, H. Tashiro, S. Ohashi, S. Nishida, and T. Tarui: *Nippon Steel Tech. Rep.*, 1995, vol. 64, pp. 45–49.
2. J.D. Embury and R.M. Fisher: *Acta Metall.*, 1966, vol. 14, pp. 147–59.
3. G. Langford: *Metall. Trans. A*, 1977, vol. 8A, pp. 861–75.
4. H Tashiro and T. Tarui: *Nippon Steel Tech. Rep.*, 2003, vol. 88, pp. 87–91.
5. V.G. Gavriljuk, V.G. Prokopenko, and O.N. Razumov: *Phys. Stat. Sol. (a)*, 1979, vol. 53, pp. 147–54.
6. J. Languillaume, G. Kapelski, and B. Baudelet: *Acta Mater.*, 1997, vol. 45, pp. 1201–12.
7. S. Goto, R. Kirchheim, T. Al-Kassab, and C. Borchers: *Trans. Nonferr. Met. Soc. Chin.*, 2007, vol. 17, pp. 1129–38.
8. C. Borchers, T. Al-Kassab, S. Goto, and R. Kirchheim: *Mater. Sci. Eng., A*, 2009, vol. 502, pp. 131–38.
9. M.H. Hong, W.T. Reynolds, Jr, T. Tarui, and K. Hono: *Metall. Mater. Trans. A*, 1999, vol. 30A, pp. 717–27.
10. M. Zelin: *Acta Mater.*, 2002, vol. 50, pp. 4431–47.
11. X. Sauvage, W. Lefebvre, C. Genevois, S. Ohsaki, and K. Hono: *Scripta Mater.*, 2009, vol. 60, pp. 1056–61.
12. K. Hono, M. Ohnuma, M. Murayama, S. Nishida, A. Yoshie, and T. Takahashi: *Scripta Mater.*, 2001, vol. 44, pp. 977–83.
13. Y.J. Li, P. Choi, C. Borchers, S. Westerkamp, S. Goto, D. Raabe, and R. Kirchheim: *Acta Mater.*, 2011, vol. 59, pp. 3965–77.
14. Y.Z. Chen, G. Csiszár, J. Cizek, C. Borchers, T. Ungár, S. Goto, and R. Kirchheim: *Scripta Mater.*, 2011, vol. 64, pp. 390–93.
15. A. Taniyama, T. Takayama, M. Arai, and T. Hamada: *Scripta Mater.*, 2004, vol. 51, pp. 53–58.
16. R.W. Cahn and P. Haasen: *Physical Metallurgy*, fourth, revised and enhanced ed., Elsevier, Amsterdam, 1996, pp. 1589–94, 1642–43, 1623–25, 1921–23, 2016–22, and 2043–50.
17. J. Wilde, A. Cerezo, and G.D.W. Smith: *Scripta Mater.*, 2000, vol. 43, pp. 39–48.
18. X. Sauvage, X. Quelennec, J.J. Malandain, and P. Pareige: *Scripta Mater.*, 2006, vol. 54, pp. 1099–1103.
19. T. Ungár, M.G. Glavicic, L. Balogh, K. Nyilas, A.A. Salem, G. Ribárik, and S.L. Semiatin: *Mater. Sci. Eng., A*, 2008, vol. 493, pp. 79–85.
20. F. Becvar, J. Cizek, and I. Prochazka: *Appl. Surf. Sci.*, 2008, vol. 255, pp. 111–14.
21. I. Prochazka, I. Novotny, and F. Becvar: *Mater. Sci. Forum*, 1997, vols. 255–257, pp. 772–74.
22. J. Cizek, M. Vlcek, and I. Prochazka: *Nuclear Instrum. Methods Phys. Res. Sect.*, 2010, vol. A 623, pp. 982–94.
23. A. Revesz, T. Ungár, A. Borbély, and J. Lendvai: *Nanostruct. Mater.*, 1996, vol. 7, pp. 779–88.
24. T. Ungár and A. Borbély: *Appl. Phys. Lett.*, 1996, vol. 69 (21), pp. 3173–75.
25. T. Ungár and G. Tichy: *Phys Phys. Stat. Sol. (a)*, 1999, vol. 171, pp. 425–34.
26. L. Balogh, G. Ribárik, and T. Ungár: *J. Appl. Phys.*, 2006, vol. 100, pp. 0235121–10.
27. G. Ribárik, J. Gubicza, and T. Ungár: *Mater. Sci. Eng.*, 2004, vols. A387–A389, pp. 343–47.
28. http://www.renyi.hu/cmwp/.
29. S. Takaki, T. Tsuchiyama, K. Nakashima, H. Hidaka, K. Kawasaki, and Y. Futamura: *Met. Mater. Int.*, 2004, vol. 10, pp. 533–39.
30. X. Zhang, A. Godfrey, X. Huang, N. Hansen, and Q. Liu: *Acta Mater.*, 2011, vol. 59, pp. 3422–30.
31. T. Ungár, I. Dragomir, A. Révész, and A. Borbély: *J. Appl. Crystallogr.*, 1999, vol. 32, pp. 992–1002.
32. T. Ungár, J. Gubicza, A. Borbély, and G. Ribárik: *J. Appl. Crystallogr.*, 2001, vol. 34, pp. 298–310.
33. M.J. Puska and R.M. Nieminen: *J. Phys. F: Met. Phys.*, 1983, vol. 13, pp. 333–46.
34. A. Hempel, M. Hasegawa, G. Brauer, F. Plazaola, M. Saneyasu, and Z. Tang: *Proceedings of the Ninth International Conference on Environmental Degradation of Materials in Nuclear Power Systems – Water Reactors*, August 1–5, 1999, Newport Beach, CA, S. Bruemmer, P. Ford, G. Was, eds., The Minerals, Metals and Materials Society, Warrendale, Pennsylvania, 1999.
35. R.N. Wes: *Positrons in Solids*, Hautojärvi P, ed., Springer, Berlin, 1979.
36. A. Vehanen, P. Hautojärvi, J. Johansson, J. Yli-Kauppila, and P. Moser: *Phys. Rev. B*, 1982, vol. 25 (2), pp. 762–80.
37. R.M. Nieminen and J. Laakonen: *Appl. Phys.*, 1979, vol. 20, pp. 181–84.
38. T.M. Hall, A.N. Goland, and C.L. Snead, Jr.: *Phys. Rev. B*, 1974, vol. 10, pp. 3062–74.
39. T.M. Hall, A.N. Goland, K.C. Jain, and R.W. Siegel: *Phys. Rev. B*, 1975, vol. 12, pp. 1613–19.
40. E. Gramsch and K.G. Lynn: *Phys. Rev. B*, 1989, vol. 40, pp. 2537–40.

41. J.A. Jackman, G.M. Hood, and R.J. Schultz: *J. Phys. F*, 1987, vol. 9, pp. 1817–31.
42. J.-E. Kluin and Th. Hehenkamp: *Phys. Rev. B*, 1991, vol. 44, pp. 11597–608.
43. J. Wolff: *Mater. Sci. Forum*, 1992, vols. 105–110, pp. 1329–32.
44. Y. Tomota, P. Lukas, D. Neov, S. Harjo, and Y.R. Abe: *Acta Mater.*, 2003, vol. 51, pp. 805–17.
45. P. Haasen: *Physical Metallurgy*, 3rd ed., Cambridge University Press, Cambridge, 1996, pp. 358–62.
46. N. Hansen: *Scripta Mater.*, 2004, vol. 51, pp. 801–06.
47. M. Zehetbauer: *Key Eng. Mater.*, 1994, vols. 97–98, pp. 287–306.
48. S.J. Zinkle, L.E.. Seitzman, and W.G. Wolfers: *Phil. Mag. A*, 1987, vol. 55, pp. 111–25.
49. A. Somoza, M.P. Petkov, K.G. Lynn, and A. Dupasquier: *Phys. Rev. B*, 2002, vol. 65, pp. 094107-1–6.
50. A. Borbély, J. Dragomir-Cernatescu, G. Ribárik, and T. Ungár: *J. Appl. Crystallogr.*, 2003, vol. 36, pp. 160–162. Link to ANIZC program: http://metal.elte.hu/anizc/.